Research Paper

The vision-based guidance, navigation, and control system of Hera's Milani CubeSat

M. Pugliatti [*], F. Piccolo, A. Rizza, V. Franzese, F. Topputo

Department of Aerospace Science and Technology, Politecnico di Milano, Via La Masa, 34, Milan, 20156, Italy

ABSTRACT

Milani is a 6U CubeSat that will be released in the Didymos binary asteroid system by ESA's Hera spacecraft. Its objectives are to study and characterize the system's asteroids, thus demonstrating the use of miniaturized technologies for asteroid science. Milani adopts sophisticated vision-based technologies for the guidance, navigation, and control system in the asteroid's close-proximity environment. This work elaborates on the architecture design and on the performance analysis of the image processing and the guidance, navigation, and control system of Milani, showing that they can successfully assure adequate pointing and control of the CubeSat in the Didymos environment.

1. Introduction

Small bodies are remnants of the primordial Solar System and they can provide invaluable information about its evolution. Bodies like asteroids and comets have been considered as targets for several space exploration missions in the past years. Rosetta was the first mission to rendezvous and study a comet [1], Hayabusa 1 explored the Itokawa asteroid [2], Hayabusa 2 performed a sampling of the Ryugu asteroid [3], and Osiris-Rex sampled the Bennu asteroid [4]. Many other missions are planned in the near future [5–8], some of them [9,10] pivoting on the use of small platforms.

Near-Earth Asteroids (NEA) are characterized by orbital parameters close to those of Earth, making them accessible targets even with low-cost and small platform missions. CubeSats, which are modular miniaturized spacecraft of several units (1 unit is a box of 10 cm edge), are revolutionizing the way Solar System exploration is made by diversifying and complementing the scientific objectives of larger missions [11,12]. CubeSats can be exploited as opportunistic payloads to be deployed in situ once the main spacecraft has reached its target. This approach is adopted in the Asteroid Impact and Deflection Assessment (AIDA) collaboration between the National Aeronautics and Space Administration (NASA) and the European Space Agency (ESA) to study and characterizes an impact with the Didymos asteroid system [13].

As part of this collaboration, NASA launched the Double Asteroid Redirection Test (DART) kinetic impactor spacecraft [14,15], whose impact with the secondary asteroid of 65803 Didymos has been observed by LICIACube in 2022 [16]. In October 2024, ESA will launch the Hera mission to carry out scientific investigation on the dynamical

and geological properties of the binary system [6,17]. Hera will release two 6U deep-space CubeSats, named Juventas [18] and Milani [19], to map and characterize the Didymos system. They will be the first interplanetary CubeSats to execute long-term operations in the close proximity of a binary asteroid system. The nominal duration of both missions is set to 90 days, with a back-up option for a further 90 days extension.

This paper elaborates on the design of the Guidance, Navigation, and Control (GNC) and Image Processing (IP) architectures of the Milani CubeSat mission and reports their performance in the environment of the Didymos binary system. The design of the system reflects its status in Summer 2022, at the end of Phase C. The specific contribution of this work is to address the use of miniaturized technologies for semi-autonomous vision-based position determination and maneuvering for a deep-space CubeSat with respect to a binary system.

2. Overview of the Milani mission

Milani is a 6U CubeSat that will be released in the Didymos environment by the Hera mothercraft in early 2027. Milani will be released during a dedicated Hera operational phase after an early characterization of the binary system. The Didymos system consists of a primary and a secondary body called Didymos (D1) and Dimorphos (D2), respectively. The former is estimated to be an irregular, spherical-like body with a diameter of 780 m while the latter is currently modeled as a tri-axial ellipsoid with a major axis of 170 m. The main scientific and technological objectives of the Milani mission are to:

Acronyms

ADCS	Attitude Determination and Control System
AIDA	Asteroid Impact and Deflection Assessment
AOCS	Attitude and Orbit Control System
CDR	Critical Design Review
CIRA	Centro Italiano per la Ricerca Aerospaziale
CoB	Center of brightness
COB	Center of brightness
CoF	Center of figure
CoM	Center of mass
CRP	Close Range Phase
DART	Double Asteroid Redirection Test
DART	Deep-space Astrodynamics Research & Technology group
D1	Didymos
D2	Dimorphos
ESA	European Space Agency
EKF	Extended Kalman Filter
EXP	Experimental Phase
FDIR	Fault detection, isolation, and recovery
FOV	Field of view
FRP	Far Range Phase
GNC	Guidance Navigation and Control
HIL	Hardware In the Loop
IMU	Inertial measurement unit
IP	Image Processing
ISL	Inter satellite link
LiDAR	Light detection and ranging
LoS	Line of sight
MC	Monte Carlo
NASA	National Aeronautics and Space Administration
NEA	Near Earth Asteroid
NIS	Normalized innovation squared
PDR	Preliminary Design Review
RAM	Random access memory
RW	Reaction wheel
SADA	Solar array driving assembly
SRP	Solar radiation pressure
SS	Sun sensor
SSTO	Sun Stabilized Terminator Orbit
SSWCOB	Sun-sensor weighted center of brightness
STM	State transition matrix
STR	Star tracker
WCOB	Weighted center of brightness

Table 1
Relevant requirements on the GNC and IP of Milani.

ID	Description
R1	The absolute pointing error during scientific acquisitions shall be lower than 0.5 deg in 1-sigma confidence.
R2	The GNC shall be able to reconstruct the spacecraft position on-board with a total error lower than 10% of the true range for 50% of the available trajectories.
R3	The IP shall be able to estimate the center of mass of D1 on-board within an error of 20 px for at least 50% of the available images.

environment and in deep-space. This objective will be fulfilled by the VISTA sensor for particle detection [21].

Demonstrate ISL communication with Hera. This targets the capability of communicating with a data-relay spacecraft for payload and platform data transmission in deep-space with a CubeSat.

Demonstrate the use of CubeSat technologies in deep-space. This includes the capability of flying a CubeSat in an asteroid environment, determining the position with vision-based methods and showing the use of miniaturized technologies in a harsh environment.

To accomplish these objectives, Milani is designed with both orbital and attitude control capabilities. The platform is a 6U CubeSat with deployable solar arrays. In addition to ASPECT, VISTA, and the ISL antennas, Milani will be equipped with a wide field of view (FOV) navcam, a light detection and ranging (LiDAR), two sun sensors (SS), a star tracker (STR), an inertial measurement unit (IMU), thrusters and a set of reaction wheels (RW). The IP and GNC have been designed to meet specific requirements. The ones which are applicable to the work presented in this paper are briefly summarized in Table 1.

The Milani mission consists of several phases, which are: (1) ejection from the mothercraft and commissioning; (2) transfer to the operational phase, where the CubeSat is guided towards achieving operational orbit; (3) the Far Range Phase (FRP), where Milani acquires images of the asteroids from far range; (4) the Close Range Phase (CRP), where the CubeSat gets closer observations of the asteroids by flying high-risk orbital arcs; (5) the Experimental Phase (EXP) where the CubeSat will orbit on a Sun Stabilized Terminator Orbit (SSTO); (6) a decommissioning phase where Milani will either be injected into a heliocentric graveyard orbit or will attempt a soft landing on D2.

This work focuses on the architecture design and performance analysis of the vision-based GNC system in the two main operative phases of Milani, namely the FRP and CRP. The Milani trajectories in these phases are strongly influenced by the effect of the binary system gravity and solar radiation pressure (SRP) perturbation [19,22]. As a result, Milani's trajectories have been designed to develop above the Didymos system exploiting hyperbolic arcs. These are represented in Fig. 1 in the W reference frame, which is centered on D1 and whose Z-axis is aligned with its spin axis, while the X and Y-axes are co-planar with the orbital plane of D2, with the X-axis following the projection of the Sun in such plane. Note that for simplicity, the same color code associated to each arc of the FRP and CRP illustrated in Fig. 1 will be used across the paper to represent properties and performance of various algorithms. The FRP and CRP last 21 and 35 days, respectively. The FRP alternates 3 and 4-days arcs, while in the CRP there are also 7-day arcs. This is done since in the CRP the CubeSat gets significantly closer to the system than the FRP, so additional trajectory correction maneuvers are necessary in the middle of the arc. The portions of an arc in the CRP before and after the correction maneuver will be referred to as a and b, respectively. The FRP exhibits symmetrical arcs that develop within 9–14 km from D1, while the CRP is constituted by asymmetrical arcs with a range of 3–22 km from the system. Fig. 2 shows the evolution of the range from D1 and of D1's phase angle (Sun-asteroid-spacecraft angle) during the two main phases.

The Milani consortium is composed of entities and institutions from Italy, Czech Republic, and Finland. The consortium prime is Tyvak
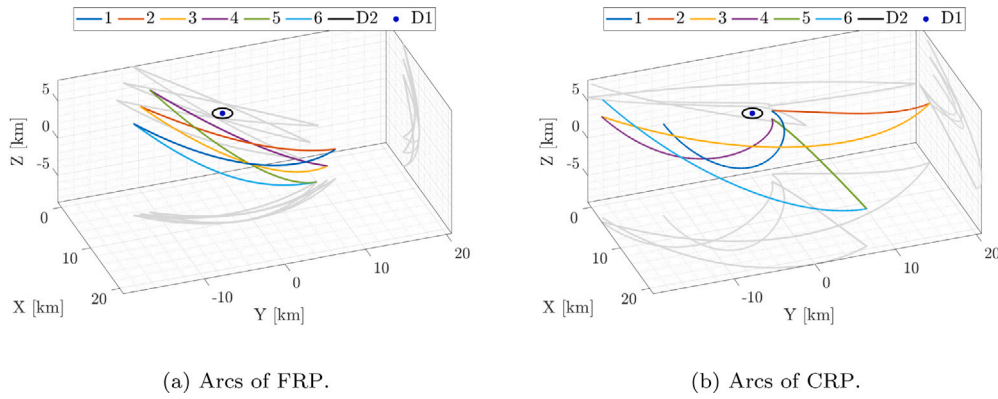
Characterize the Didymos binary system. This includes supporting Hera for the determination of the system extrinsic properties, characterization of the asteroids' surfaces, evaluation of space weathering phenomena, and characterization of the DART crater region. This objective will be achieved by a global mapping of D1 and D2 with high-resolution images of both bodies with the ASPECT payload [20].

Estimate the gravity field. The range and range-rate measurements exchanged between Milani and Hera via the Inter Satellite Link (ISL) are exploited to estimate the gravity field in the asteroid environment.

Characterize the dust environment. This includes the detection of inorganic materials, volatiles, and light organics both within the asteroid

(a) Arcs of FRP.

(b) Arcs of CRP.

Fig. 1. Milani's nominal trajectories. Gray lines represent the projections into the XY, XZ and YZ planes. (For interpretation of the references to color in this figure legend, the reader is referred to the web version of this article.)
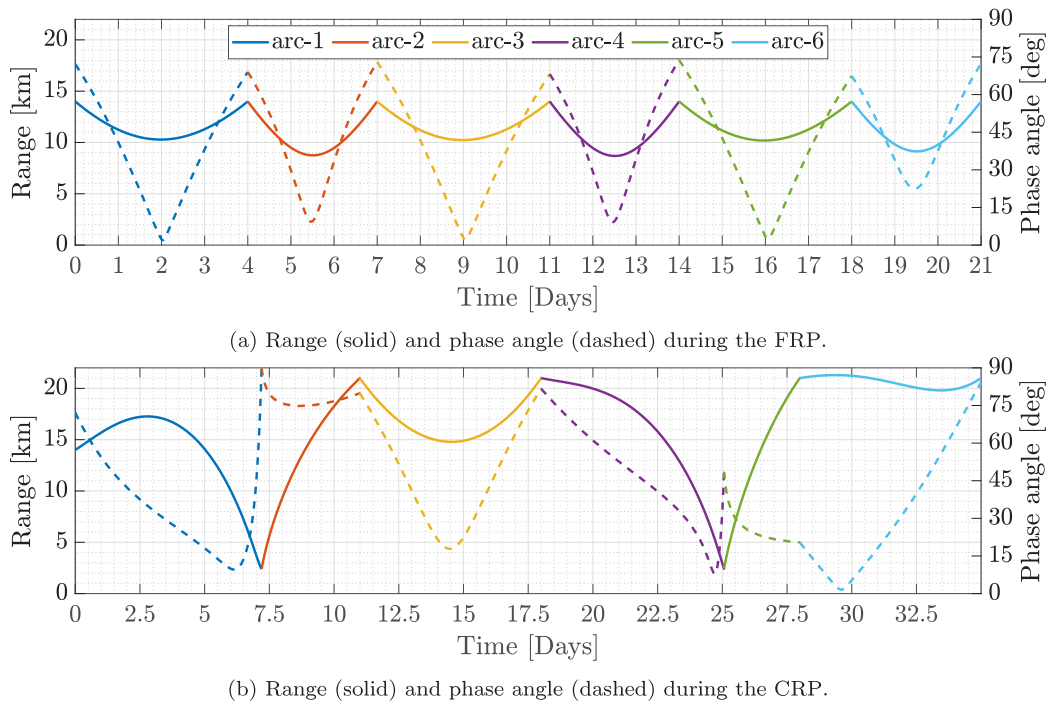

(a) Range (solid) and phase angle (dashed) during the FRP.

(b) Range (solid) and phase angle (dashed) during the CRP.

Fig. 2. Geometric properties of FRP and CRP.

International, which is responsible for the whole program management and platform design, development, integration, testing, and final delivery to the customer. Politecnico di Torino has worked on the requirements definition, thermal analysis, radiation analysis, and debris analysis. Politecnico di Milano is responsible for Mission Analysis and GNC. Altec is supporting the ground segment architecture and interface definition. The Centro Italiano per la Ricerca Aerospaziale (CIRA) is responsible for the execution of the vehicle environmental test campaign. HULD contributes to the development of mission-specific software. VTT is the main payload (ASPECT) provider, and it is supported by the following entities dealing with ASPECT-related development: the University of Helsinki (for the calibration), Reaktor Space Lab (for the development of the Data Processing Unit), Institute of Geology — the Czech Republic Academy of Science (scientific algorithms requirements and testing), and the Brno University of Technology (scientific algorithms development). INAF-IAPS is the secondary Payload (VISTA) provider.

Throughout its design, the Milani mission has been characterized by a fast development cycle. Phase 0 took place during proposal preparation in spring 2020. The Milani team successfully passed the

Preliminary Design Review (PDR) in summer 2021 and the Critical Design Review (CDR) in spring 2022, and it is currently in phase D.

3. Design

The GNC of Milani is designed as a semi-autonomous vision-based system with the primary purpose of generating a reliable, simple, and accurate primary pointing to the Attitude Determination and Control System (ADCS) during the different scenarios of the mission. In order to do so, Milani's GNC exploits strategies based on IP algorithms that extract optical observables from images of the binary system.

The GNC and ADCS are two separate systems, but they are deeply connected. Together, they form the Attitude and Orbit Control System (AOCS), which is responsible for the full six-degree-of-freedom orbital and attitude navigation, guidance, and control of the CubeSat. Since the GNC system generates autonomously an on-board primary pointing profile as output for the rotational motion, and since it does not have on-board autonomy on the translational guidance and control, the system is defined as semi-autonomous. The overall architecture of the
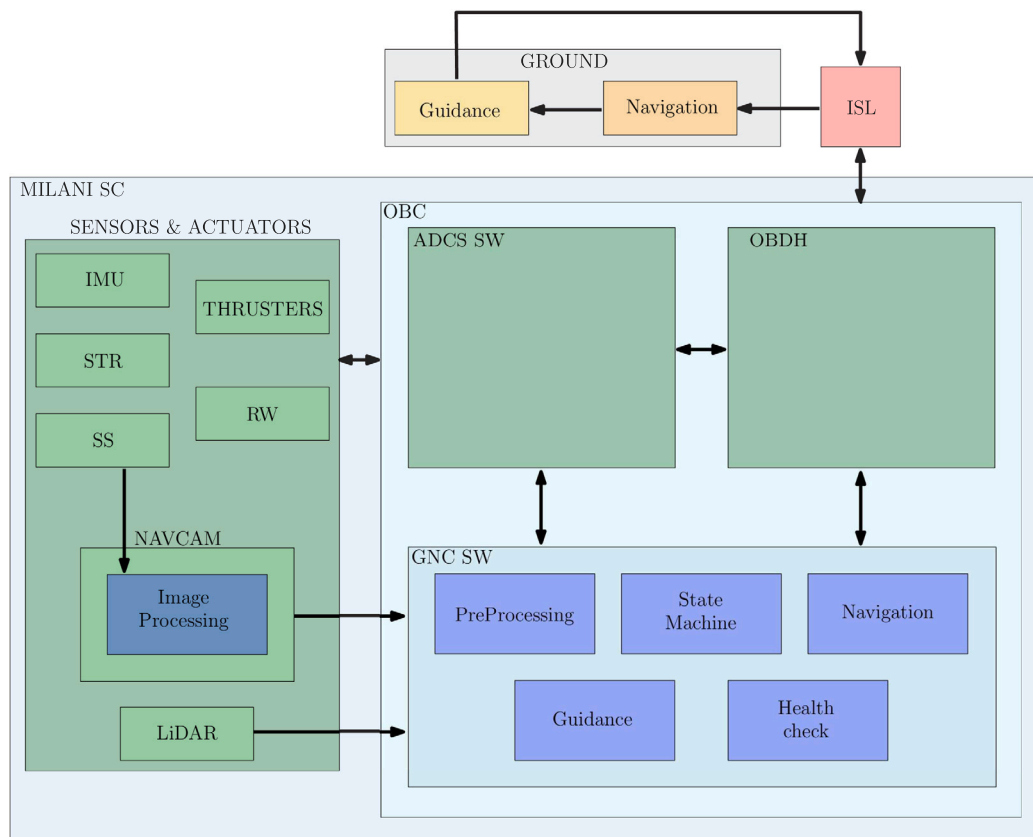
Fig. 3. High-level architecture of the AOCS system of Milani. The areas highlighted in blue are the focus of this work. (For interpretation of the references to color in this figure legend, the reader is referred to the web version of this article.)

AOCS is represented in Fig. 3, where the connections between the GNC, the ADCS and the rest of the system are visualized.

Both the GNC and IP have been developed by the Deep-space Astrodynamics Research & Technology group (DART)[1] at Politecnico di Milano using Simulink 2020a[2] for its simplicity and the capability to convert high-level rapid prototyping code in Matlab/Simulink as C-code via auto-coding. This capability allows for fast iteration between the design of the algorithms and their integration with the on-board software.

In the following sections, the design of the IP and GNC systems is illustrated in detail. Note that their architectures have been primarily influenced by the specific needs of the FRP and CRP phases, which allow the achievement of all scientific and technological objectives of the Milani mission. The EXP is considered an opportunistic phase of the mission and thus does not influence the overall design of the IP and GNC systems.

3.1. Design of the image processing

Milani's on-board navigation strategy relies on optical observables of D1 extracted from images and then used in an on-board Extended Kalman Filter (EKF). To do so, a robust, simple, and accurate IP method is needed. For the case of Milani, information must be extracted from D1 for navigation, but at the same time, D2 must be clearly distinguished in the image for pointing purposes. This is because D1 is the optimal target for navigation purposes, since it is the largest, most visible, and regular body of the binary system. On the other hand, D2

is the scientific focus of the mission, and therefore it is important to distinguish it from D1 for dedicated scientific data acquisition.

A detailed description of the IP can be found in [23,24], thus in this work only a brief overview is given. The interested reader is also directed to [25] for an assessment of the algorithm performance within a Hardware-In-the-Loop (HIL) setup. Milani's IP is made of 5 blocks, as illustrated in Fig. 4. The *PreProcessing, State Machine*, and *PostProcessing* ones handle internal logics, while the *Blobs Characterization* and *Observables Extraction* blocks represent the algorithmic core of the IP.

The input to the IP is a set of data and configuration parameters, while the output is a state vector that contains optical observables and quantities extracted from images. These include the estimated center of mass (CoM), also referred to as center of figure (CoF), of D1 and D2 (respectively $(CoF)_{D1}$ and $(CoF)_{D2}$), the number of bodies detected in the image (f), the estimated phase angle (Ψ), the range from D1 (ρ), and finally a set of flags and consistency checks passed outside towards other subsystems (v_1, v_2 for the consistency of the IP and the asteroid detection, respectively, and γ_{ip} as the effective operative mode of the IP). Note that assuming a homogeneous body, as considered in this work, a correct estimate of the CoF would coincide with the CoM. A shift exits if considering a non-homogeneous mass distribution, irrespective of the accuracy of the estimate of the CoF.

Once an image is received by the IP, the first meaningful block in which algorithmic operations are performed is the *Blobs Characterization* one. Its purpose is twofold: to distinguish between D2 and D1 in the image, and to extract low-level geometrical properties about the blob of pixel of the latter. The *Blobs Characterization* flowchart is illustrated in Fig. 5.

The starting point is the image generated by the navcam, which, in the simulation environment, is generated in Blender[3] according to the
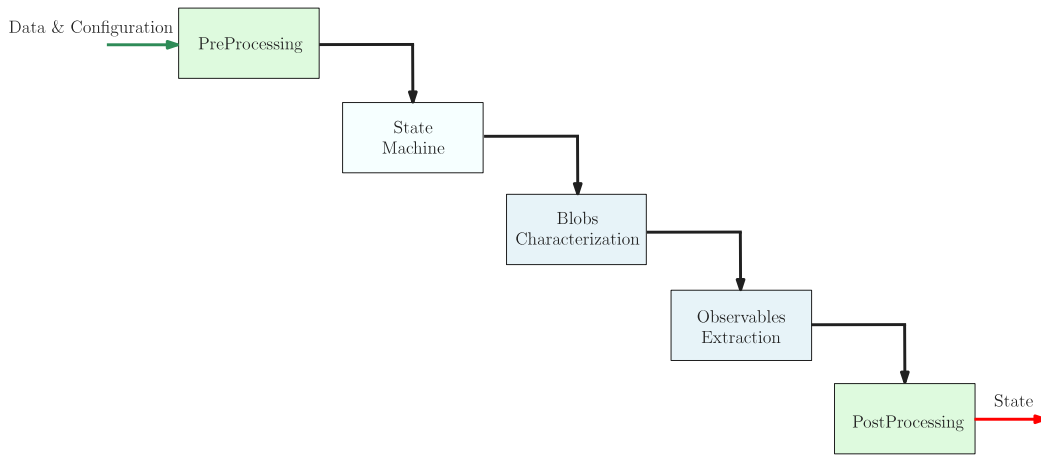

Fig. 4. High-level architecture of the IP software.

Table 2
Operative modes γ_{ip} of the IP.

Mode	Description
NOP	No operations are performed by the IP.
COB	The CoF is estimated as the centroid of the blobs of pixels associated to D1.
WCOB	A data-driven scattering law based only on optical observables is used to generate the CoF by correcting the CoB.
SSWCOB	A data-driven scattering law based on optical observables and data from the SS is used to generate the CoF by correcting the CoB.

noise characteristics expected in the Milani mission case. The first step is image binarization, which transforms the grayscale array into a logic one. Next, morphological operations are performed to reduce the number of blobs of pixels generated by the binarization step and to smooth their geometrical appearances. Opening, closing, or no operation can be performed on the images via a user-defined structuring element in the form of a kernel. This provides great flexibility during operations since the kernel can be easily updated as a configuration parameter of the IP. Blob analysis is then performed to construct a characteristic feature vector for each blob of pixels. The elements constituting this vector are: area, bounding box (Γ), center of brightness (CoB), eccentricity (e) and major axis length (δ) of the ellipse fitted to each blob of pixels. These elements are used as input by the object recognition function, which is used to detect the number of bodies in the image, distinguish between D1 and D2, and finally generate low-level geometric observables about them. D1 is recognized as the biggest blob of pixels in the image, while D2 is recognized exploiting the area outside of an expanded Γ, a newly computed expanded bounding box, Γ^{ex}, which as the name suggests is an expanded version of the original bounding box around D1.

The low-level optical observables are further refined for D1 with the use of more sophisticated algorithms in the *Observables Extraction* block (flowchart in Fig. 6. Its key characteristic is the presence of three branches which reflect different operative modes γ_{ip} of the IP that are summarized in Table 2.

The first and simplest of them is represented by the center of brightness (COB) branch, which simply outputs the (CoF)$_{D1}$ as the CoB computed from the blob analysis performed in the previous block. Note that in this paper the notation CoB refers to the centroid of the blobs of pixels, while COB refers to the algorithm branch illustrated in Fig. 6. This strategy is expected to perform poorly at high phase angles, where the distance between the CoB and the CoM projected into the image plane can be significant. To overcome this limitation and provide an accurate estimate of the CoM under different geometric conditions, two other strategies are implemented in the weighted center of brightness (WCOB) and sun-sensor weighted center of brightness (SSWCOB) branches.

In the WCOB a set of data-driven functions is used to shift the CoB position in the image plane towards the CoM. The magnitude and orientation of the correction vector are based solely on geometric observables extracted from images, which are also exploited to estimate the phase angle Ψ and the range ρ. For this approach to work, a database is generated offline to represent the possible geometric conditions that could be encountered considering the envelope of the Milani trajectories. The images from this database are used to tune the coefficient of the data-driven functions used by the WCOB. These functions are not described here in detail, but the interested reader is directed towards [23,24] for additional information. The decision to employ a data-driven scattering law is motivated by the irregular shape of D1 and by the simplicity to adapt the algorithm to its real shape once it is imaged, first by the Dart spacecraft in 2022 and then by Hera in 2027, before Milani's release.

A similar approach is employed by the SSWCOB, with the major difference that data from the SS is used together with data extracted from the image. Because the former is more accurate than the latter in predicting Ψ, the SSWCOB is capable of higher performance. However, it also makes this strategy depend on the availability of the external data other than images. Both branches shift the CoB using Eq. (1):

$$\begin{bmatrix} CoF_x \\ CoF_y \end{bmatrix} = \begin{bmatrix} CoB_x \\ CoB_y \end{bmatrix} + \omega \cdot \mu(\Psi, \delta) \cdot \begin{bmatrix} \cos(\Phi) \\ \sin(\Phi) \end{bmatrix} \qquad (1)$$

where Ψ is the phase angle, μ is the magnitude in pixels of the correction vector between CoB and CoM, Φ is an orientation function and ω is a weight vector that can be used to tune the correction term. In all operative modes of the IP, the range is estimated in the same way using a trivial apparent diameter formula that can be corrected from ground with a bias term.

3.2. Design of the guidance, navigation, and control system

The main task of the GNC system is to provide a primary pointing direction to the ADCS. During most of the mission, the primary pointing coincides with the pointing of the navcam, the LiDAR, and ASPECT, which are all mounted co-axially. However other constraints could also be verified. For example, it may be desired to direct one of the ISL antennas towards Hera. Furthermore, the GNC produces an estimate of the spacecraft state, intended as its position and velocity in the inertially fixed *ECLIPJ2000* reference frame, centered on the system barycenter. In addition to being used for navigation purposes, this estimate can be used to derive the primary pointing from simple geometric considerations.

A generic overview of the GNC design before CDR is briefly illustrated in [26], while in this paper the architecture is illustrated in more detail. The GNC is composed of 5 blocks, as illustrated in Fig. 7.
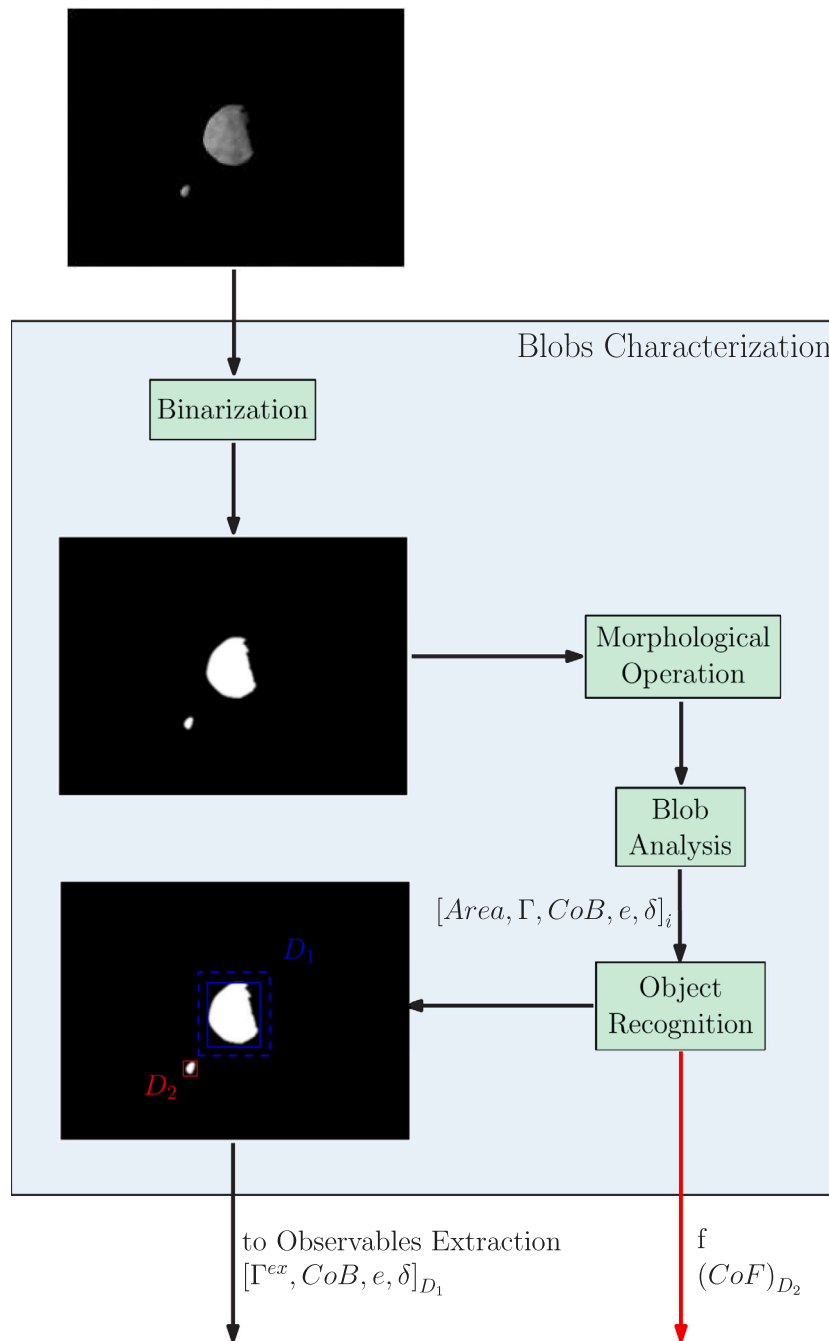
Fig. 5. High-level architecture of the *Blobs Characterization* block of the IP.

The first is the *PreProcessing* one, which performs initial checks on the input variables to ensure their validity. These include freshness checks to make sure that incoming signals have been updated recently enough and integrity checks to verify that the values are received within expected intervals. Thereafter, the *State Machine* determines the appropriate operative mode based on pre-defined logic. Then, the *Navigation* and *Guidance* blocks follow, in which optical observables and on-board ephemerides are used to compute the desired pointing profile. The validity of the navigation and guidance output is verified in the *Health check* block before being provided to the rest of the system as an output state vector.

The functionalities of the GNC system are defined by 5 different operative modes γ_{gnc}, described in Table 3. These are devised to communicate the status of the GNC to other systems. Furthermore, a set of navigation, guidance, and EKF submodes are defined, indicated by γ_{nav}, γ_{gui}, γ_{ekf} respectively. The latter are used to determine the specific algorithms executed within each block and are computed before γ_{gnc}.

The modes are selected according to a series of truth tables that check a set of logic conditions based on the input signals and the checks computed within the *PreProcessing* block. In all cases, the default mode is always the simplest one and, if the necessary conditions are met, the system automatically escalates to more complex ones. The only exception is represented by the *Asteroid Search* mode, which is intended as a contingency option and therefore requires ground intervention and cannot be activated autonomously on-board. It is also noted that the highest reachable mode can be limited from ground using a set of configuration parameters.
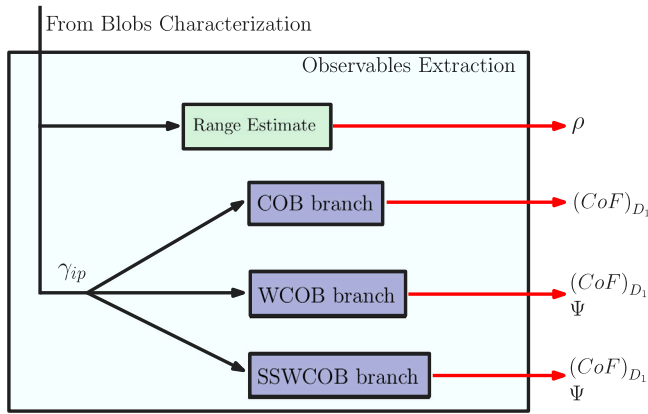
Fig. 6. High-level architecture of the *Observables Extraction* block of the IP.

Table 3
Operative modes γ_{gnc} of the GNC.

Mode	Description
Drift	This mode is triggered when an issue has been detected in *Navigation* or *Guidance* blocks. In such a case neither output of these blocks is to be considered reliable.
Navigation	The best navigation strategy is targeted for execution. The output of the *Guidance* block is not considered reliable.
Guidance	The best guidance strategy is targeted for execution. The output of the *Navigation* block is not considered reliable.
Nominal	Both *Navigation* and *Guidance* blocks are executed targeting the best possible strategy. Their outputs are considered reliable.
Asteroid Search	Ephemeris-based navigation is targeted whenever possible. The guidance of the primary pointing is designed to re-acquire the target in the FOV.

3.2.1. Navigation

In the *Navigation* block the state of the CubeSat with respect to the asteroid system is estimated. The algorithms used in this block are driven by 3 different navigation submodes γ_{nav}: *Navigation keep last*, *Navigation from ephemerides*, and *Navigation from EKF*.

In *Navigation keep last*, the navigation solution is not updated and the last solution produced is kept as output. In *Navigation from ephemerides*, ephemeris data provided from ground are interpolated to estimate a navigation solution. Ephemerides are stored on-board Milani as matrices of Chebyshev polynomial coefficients associated with specific time intervals. At any given time during the mission, two sets of coefficients are stored simultaneously to represent the current and next arc of the trajectory. These are referred to as nominal and standby sets, respectively, and are updated automatically after orbital maneuvers. This strategy has a twofold purpose: to avoid degradation in the interpolation of multiple hyperbolic arcs with a single set of coefficients and to provide robustness to contingency scenarios, given that a single set can be used to cover a longer timespan. Finally, in *Navigation from EKF* the navigation solution is provided by the on-board EKF, which relies on optical observables from the IP as well as ranging data from the LiDAR to generate a state estimate.

The EKF uses a dynamical model that accounts for the gravitational effects of D1, D2, and the Sun (which are all treated as point masses), as well as for the SRP, which is modeled on-board with a simple cannonball model. The SRP acceleration is split into a deterministic and a stochastic part. Furthermore, a stochastic residual acceleration is included to account for other uncertainties in the spacecraft dynamics. Both the residual acceleration and the stochastic part of the SRP are treated as Gauss–Markov processes with the properties given in Table 4.

The equations of motion are propagated using a Runge–Kutta 4th order integrator, while the state transition matrix (STM) is computed on-board using a second order approximation:

$$\mathbf{\Phi}(t, t + \Delta t) = \mathbf{I}_{6\times6} + \mathbf{A}_{\Delta t/2} \Delta t + \mathbf{A}_{\Delta t/2}^2 \frac{\Delta t}{2} \qquad (2)$$

Table 4
Statistical properties of the residual acceleration and SRP. σ is the standard deviation of the white noise driving the Gauss–Markov process, and τ is the autocorrelation time.

	σ	τ
Residual acceleration	5×10^{-9} m/s^2	1 day
Solar radiation pressure	8% of SRP acceleration magnitude	1 day

Table 5
Standard deviations assumed for EKF measurements.

Measurement	σ
Range	15 m
CoF - COB	40 px
CoF - WCOB	20 px
CoF - SSWCOB	15 px

where $\mathbf{I}_{6\times6}$ is the 6×6 identity matrix, Δt is the propagation time, and $\mathbf{A}_{\Delta t/2}$ is the Jacobian of the equations of motion with respect to the state, evaluated at the midpoint of the propagation step [27].

The operative modes of the EKF are driven by 5 different EKF sub-modes γ_{ekf}, which depend on the available measurement: *EKF keep last*, *Propagation only*, *Propagation + lidar*, *Propagation + IP*, and *Propagation + IP + lidar*.

In *EKF keep last*, the solution is not updated and the last solution produced is kept as output. In *Propagation only* the state is propagated up to the current time, but no measurements are used in the filter. In the remaining submodes, the state is propagated and the available measurements are used in the EKF update step. The on-board filter is designed to take as input the CoF of D1 and the range measurement from the LiDAR. At the current stage of the design, other measurements are discarded since they are not considered sufficiently reliable. The CoF from the IP is used every 30 minutes and the range from the LiDAR every 5 minutes, if available. It is also noted that both the IP and LiDAR work within a specific range envelope from D1: the former is designed to work between 3 and 23 km, while the latter is assumed to work below 5.5 km.

The measurements are assumed to be affected by Gaussian random noise with 0 mean and standard deviation as given in Table 5. The 0-mean Gaussian assumption is reasonable for the range measurement and for the WCOB and SSWCOB modes of the IP. Instead, for the simple COB method, a bias in the CoF measurement is expected at high phase angles. Since this method is foreseen to be used only as a backup option and for simpler pointing purposes, the EKF has not been modified to account for this effect. It is also noted that the uncertainty used for the range measurement accounts for both the error due to the LiDAR sensor and the uncertainty of the shape of D1.

When IP measurements are available, a consistency check is additionally performed on the EKF output. Its purpose is to verify that the estimation error is consistent with the expected covariance matrix. The check is based on the normalized innovation squared (NIS) of the CoF measurement:

$$n = (\mathbf{y} - \hat{\mathbf{y}})^\top (\mathbf{H}\bar{\mathbf{P}}\mathbf{H}^\top + \mathbf{R})(\mathbf{y} - \hat{\mathbf{y}}) \qquad (3)$$

where n is the NIS, $\mathbf{y}$ is the measurement, $\hat{\mathbf{y}}$ is the EKF reference measurement, $\mathbf{H}$ is the Jacobian of the measurement with respect to the state, $\bar{\mathbf{P}}$ is the propagated covariance matrix of the state vector, and $\mathbf{R}$ is the covariance matrix of the measurements. Under the EKF's hypotheses, the NIS should follow a chi-squared probability distribution, with degrees of freedom equal to the number of measurements considered [27]. This assumption can be used to check how likely the current value of the measurements residuals is. If it is highly unlikely, some of the hypotheses are probably being violated. The consistency check is based on the CoF measurement because it is the most reliable one. However, this choice makes the evaluation insensitive to errors in the direction of the navcam boresight. To increase robustness against
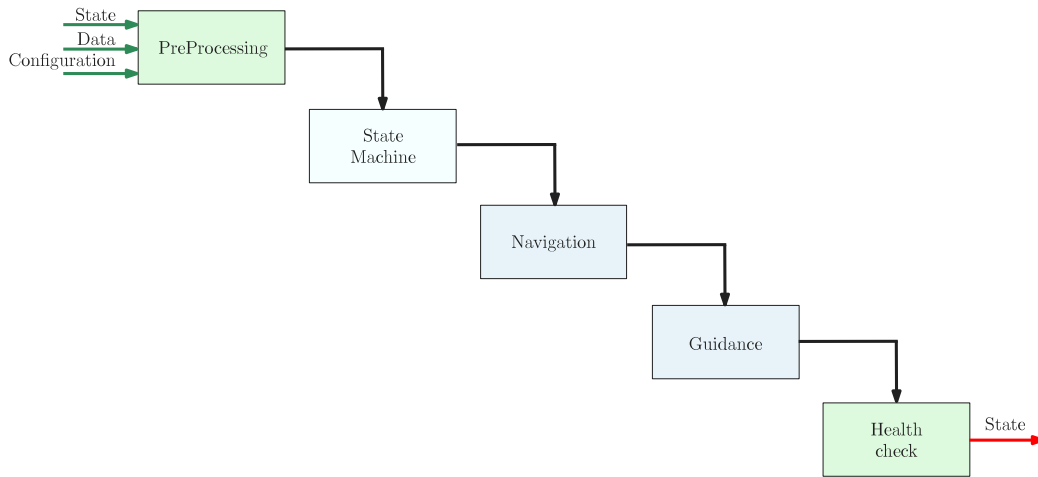
Fig. 7. High-level architecture of the GNC.

statistical fluctuations and possible measurement outliers, the consistency check relies on the sum of last three values of the NIS. This sum follows a chi-squared distribution with three times the number of degrees of freedom. Then, the cumulative distribution function of the sum is computed. If it is above a predefined threshold, the EKF output is considered invalid.

3.2.2. Guidance

The algorithms used in the *Guidance* block are driven by 5 different submodes γ_{gui}: *Guidance keep last*, *Reference*, *Tracking*, *Predicted*, and *Search pattern*.

As for the *Navigation* block, in *Guidance keep last* the last computed solution is used. In *Reference* the guidance is obtained from ground-based information, either by following a specified pointing profile or interpolating ephemerides data. In *Tracking* data from the IP is used to track the target asteroid and keep it at the center of the navcam FOV. While waiting for new IP data, a fixed inertial pointing is kept. In *Predicted* the position estimated by the EKF is combined with the ephemerides of the target body to compute a pointing solution. While in *Tracking* the target must be detectable by the IP, which limits it to either D1 or D2, in *Predicted* it can be any geometric point in the system. Finally, in *Search pattern* a contingency guidance submode is implemented to recover the target body in the navcam FOV after it has been lost. In this submode, the primary pointing is computed by following a profile obtained from a predefined map. The latter is defined relatively to the attitude determination solution available when this submode has been enabled. Different pointing profiles can be configured. Furthermore, a prohibited Sun-exclusion cone can be defined to preserve optical payloads. When the target is found, the guidance submode automatically switches to *Tracking*.

3.2.3. Fault detection, isolation, and recovery

The fault detection, isolation, and recovery (FDIR) strategy of Milani is operated by the *PreProcessing*, *State Machine*, and *Health check* blocks of the GNC. The first is in charge of detecting potential issues by checking the validity of the input variables. The second uses the results of these checks to select the suitable operative modes, adapting automatically in case of issues due to missing data or faults in other systems. Finally, the third block detects possible issues within the GNC by checking the validity of navigation and guidance solutions. In particular, it checks that they are within predefined bounds and that the pointing direction is outside of a predefined Sun exclusion angle, to avoid damage to the optical sensors. Thanks to this strategy, potential GNC issues are detected and do not propagate to the rest of the system.
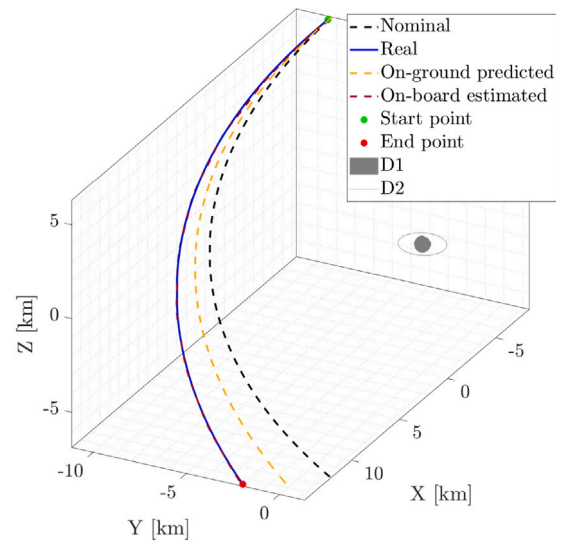

Fig. 8. Definition of Milani trajectories: Nominal, real, on-ground predicted, on-board estimated.

4. Analysis methodology

The validation and verification of Milani's IP and GNC consists of open-loop and closed-loop high-fidelity simulations performed in Matlab/Simulink within the framework developed by the DART group for proximity operation scenarios [28]. This section presents the main assumptions and illustrates the simulation framework adopted.

The analyses involve a set of different trajectories, which are illustrated in Fig. 8, together with their nomenclature. The nominal trajectory is the one designed by the mission analysis team on ground for optimality in science, safety, and flyability. The real one is the trajectory flown by the CubeSat. In this work, the latter is simulated by sampling the expected dispersion around the initial conditions of the nominal trajectory, as illustrated in [29]. The on-ground predicted and the on-board estimated are instead estimated trajectories. Specifically, the former is the one generated by the flight dynamics team propagating the orbit determination solution, while the latter is the one estimated by the on-board EKF. It is worth noting that the on-ground predicted trajectory is the one used to generate the Chebyshev coefficients to be sent to the CubeSat.

A set of extensive analyses has been performed to validate the design of the IP and GNC with a twofold objective: to confirm the expected behavior of the systems during nominal and off-nominal events (in particular attitude and orbital maneuvers, sensor faults, missing input data, and other contingency scenarios), and to assess compliance with performance requirements, which are reported in Table 1. For simplicity, these analyses are divided into five categories:

- **Static**: The performance of the IP are assessed assuming ideal pointing towards D1 in open-loop simulations with image datasets of the FRP and the CRP rendered offline.
- **Nominal**: The GNC and IP performance are assessed on the nominal trajectories by setting the highest possible modes.
- **Performance**: The performance are evaluated for different combinations of IP, navigation, and guidance submodes which are constant during the entire trajectory. Dispersed trajectories simulate real ones and are used to assess the response to uncertainty in the initial conditions of each arc with different strategies.
- **Monte Carlo**: A test campaign of 100 simulations is performed on dispersed trajectories on selected arcs.
- **Logics**: Failures and critical events are simulated to test the correctness of the internal logics.

In the static assessment of the IP, two datasets of 12101 and 20164 images have been generated from the FRP and CRP trajectories, respectively, sampled every 150 seconds. In these datasets, ideal pointing towards D1 is assumed as well as fixed secondary pointing aligned with the Z-axis of the W reference fame. These conditions are not respected during closed-loop simulations because of pointing error and different assumptions on the secondary pointing. However, since the IP algorithms are designed to be both rotation and translation invariant, these assumptions are kept to simplify the analyses over the static datasets.

Dispersed trajectories represent possible real ones and are generated by the mission analysis team using a surrogate model of the on-ground orbit determination process [29]. Surrogate models are also used to simulate the ADCS and the actuators. The former follows the primary pointing provided by the GNC with a realistic profile that considers maximum Sun exposure for the solar panels as well as control of the solar array drive assembly (SADA). Inside the surrogate model, the estimated angular velocity and spacecraft attitude are affected by Gaussian noises respectively of 0.01 deg/s and 30 arcsec, both at 1σ. Similarly, the true pointing error and pointing stability are modeled perturbing the target attitude with a tuned Gauss–Markov process noise having sigma of 46 arcsec and characteristic time of 2 s. On the contrary, the estimated Sun direction, being fed directly into the GNC keeps the accuracy of the sensors, namely 3.67 deg at 1σ on each axis. It is noted that during flight operations it will be possible to uplink to the CubeSat estimated initial conditions and maneuvers for each arc. These will be used to initialize the on-board navigation filter at the beginning of each arc.

The verification and validation campaign of the Milani IP and GNC up to the mission CDR comprehends a vast set of analyses. This paper reports only a subset of illustrative examples which represent the level of performance achieved. In particular: 1) a global static assessment of the IP is presented for both the FRP and CRP; 2) a global on-board navigation performance assessment is illustrated on the nominal trajectories in all arcs of the FRP and CRP; 3) an example of performance assessment is illustrated on arc 4b of the CRP. This arc is chosen since it represents a challenging traverse over the Didymos environment in which the CubeSat gets very close to the system; 4) two Monte Carlo (MC) campaigns are illustrated for arc 1 of the FRP and arc 1b of the CRP; 5) an example of logic assessment to show the autonomous transition capabilities of the GNC.

Table 6
Performance metrics of the IP strategies in the *FRP* and *CRP* datasets.

	Metric	COB	*FRP* WCOB	SSWCOB	COB	*CRP* WCOB	SSWCOB
ε_α	μ [%]	9.75	2.93	2.06	10.90	3.36	2.12
	σ [%]	6.09	2.21	1.29	7.49	3.00	1.40
ε_ψ	μ [deg]	n.a.	0.99	0.35	n.a.	1.03	0.31
	σ [deg]	n.a.	6.96	3.68	n.a.	6.40	3.67
ε_ρ	μ [m]	333.12	333.12	333.12	539.44	539.44	539.44
	σ [m]	426.33	426.33	426.33	614.65	614.65	614.65

5. Results

This section shows the performance of the IP and GNC in the most representative cases for Milani, according to the categories reported in Section 4. The performance of the IP for the COB, WCOB, and SSWCOB strategies are compared over the FRP and CRP static datasets considering the following metrics:

$$\varepsilon_\alpha = \varepsilon_{CoF}^n \cdot \frac{\beta}{AS} \cdot 100 \quad ; \quad \varepsilon_\psi = \psi^e - \psi^t \quad ; \quad \varepsilon_\rho = \rho^e - \rho^t \quad (4)$$

where ε_α is the CoF-CoM error expressed as relative error in angular size with respect to the size of D1, ε_ψ is the error of the phase angle estimate, ε_ρ is the error of the range estimate, β is the instantaneous FOV, AS is the apparent size of D1, ε_{CoF}^n is the distance in pixel in the image plane between the estimated and true CoM, ψ^e and ρ^e denote the estimated phase angle and range, respectively, while ψ^t and ρ^t denote their true values.

The performance of the GNC is instead evaluated using the following metrics:

$$\varepsilon_\mathbf{p} = \mathbf{p}^e - \mathbf{p}^t \quad ; \quad \varepsilon_\mathbf{v} = \mathbf{v}^e - \mathbf{v}^t \quad ; \quad \varepsilon_\theta = \mathrm{acos}(\mathbf{u}_M \cdot \mathbf{u}_{D1}) \quad (5)$$

where $\varepsilon_\mathbf{p}$ and $\varepsilon_\mathbf{v}$ are the position and velocity estimation errors, ε_θ is the pointing error, $\mathbf{p}^e$, $\mathbf{v}^e$ and $\mathbf{p}^t$, $\mathbf{v}^t$ are respectively the estimated and true position and velocity components of the Milani state vector, while $\mathbf{u}_M$ and $\mathbf{u}_{D1}$ are the line of sight (LoS) of Milani's payloads and the LoS to the CoM of D1, respectively.

The performance is better visualized using the camera frame, whose origin is centered in the camera mounting position on the CubeSat, the Z-axis represents the boresight direction, and the X and Y-axes are aligned respectively with the longest and shortest size of the sensor.

5.1. Static

The static category assesses the performance of the IP for both the FRP and CRP. Table 6 summarizes the performance of the various IP modes in the two static test datasets, where μ and σ denote the mean value and the standard deviation, respectively.

From the values of ε_α, it is immediately possible to appreciate the beneficial effect of the data-driven scattering laws in the WCOB and SSWCOB methods over the simple COB. It is also noted that the SSWCOB performs slightly better than the WCOB. The error on the phase angle estimate ε_ψ is less spread when using data from the SS than when using the direct estimation from images. This in turn is reflected in the better performance seen in ε_α. Lastly, it is possible to see that the range estimate is characterized by a large error, both in terms of mean and variance, which makes such quantity less reliable for other systems outside the IP.

For completeness, the performance of ε_α for the three strategies over the entire FRP and CRP datasets are illustrated in Fig. 9. For clarity, the same color code used in Fig. 1 to represent the arcs is adopted by the background areas. Note that, while globally the SSWCOB and WCOB perform better than the COB, as discussed previously, there exist local spots in which this is not true. When comparing Figs. 9 with 2, it is possible to see that these are linked to cases at low phase angle, when
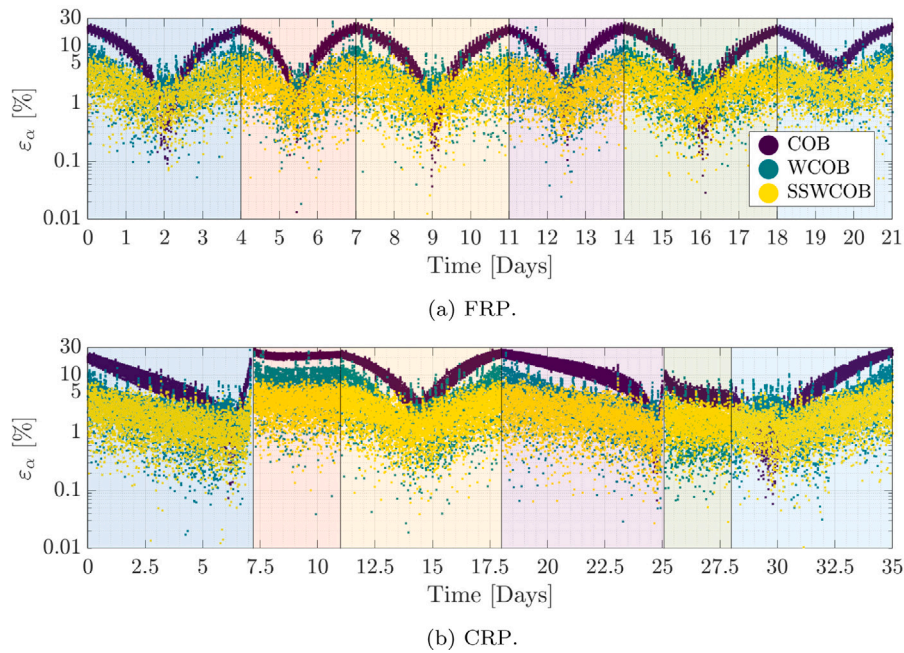
(a) FRP.

(b) CRP.

Fig. 9. ε_a for different IP strategies.
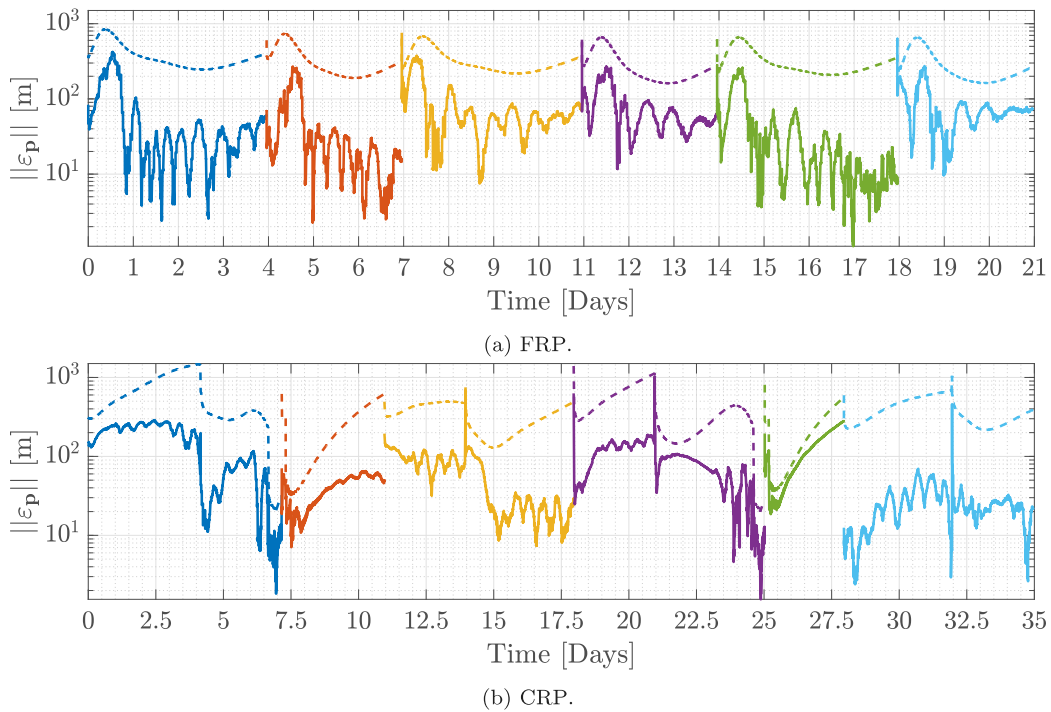

(a) FRP.

(b) CRP.

Fig. 10. EKF position estimation error during FRP and CRP. Solid line: error, dashed line: 3-sigma bounds.

D1 is fully visible. In such cases, the application of the scattering law is less effective than the simple CoB. It is also noted that the performance improvement is negligible in absolute terms, as the error on ε_a in these cases is less than 1%.

5.2. Nominal

The EKF performance achieved when using the SSWCOB algorithm and LiDAR measurements in nominal conditions are illustrated in Fig. 10 for the entire FRP and CRP. This scenario represents the case in which both the GNC and IP are performing at the best of their capabilities and Milani is considered to be flying on the nominal trajectory.

As seen in Fig. 10, in the vast majority of the arcs the EKF solution converges quickly to small errors and always stays within the 3σ bounds, depicted by the dashed lines. The discontinuities between different arcs are due to the fact that the EKF is reinitialized at the beginning of each arc. The geometric variability of the CRP arcs makes
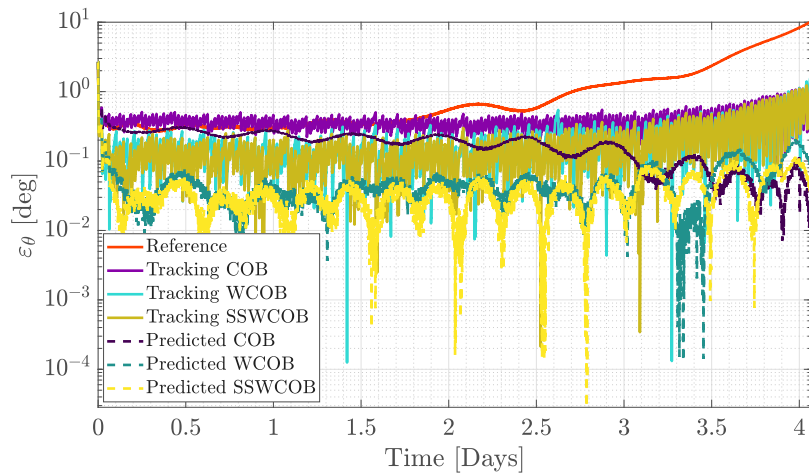
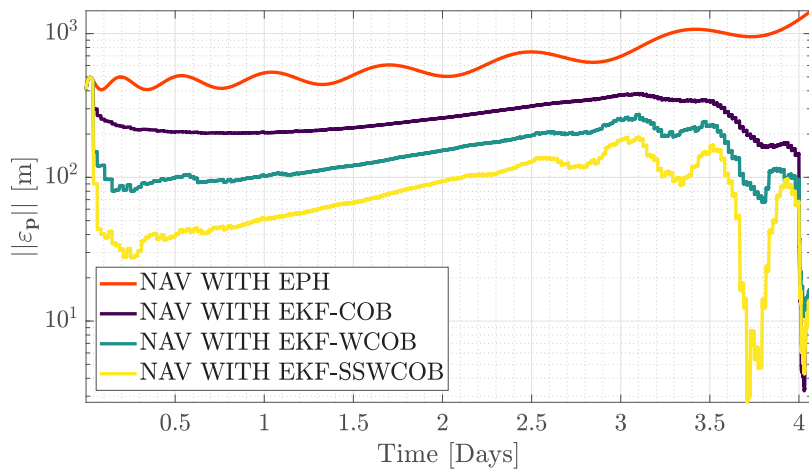**Fig. 11.** Pointing error for each combination of guidance and IP modes.

Fig. 12. Position estimation error for each combination of navigation and IP modes.

it a more challenging phase than the FRP, as seen from the high variability of the error from arc to arc in the former.

5.3. Performance

The arc 4b of the CRP is selected as an example of performance assessment. Various combinations of guidance strategies (*Reference*, *Tracking*, or *Predicted*) are coupled with different IP modes (COB, WCOB, or SSWCOB) to assess which one works best with regard to pointing and on-board state reconstruction concerns.

From the pointing error perspective, in Fig. 11 can be seen that the pointing strategies based on the use of the EKF outperform the other ones. Overall, the *Predicted WCOB* and *Predicted SSWCOB* are the ones performing best in this scenario, followed by *Tracking WCOB* and *Tracking SSWCOB*. For most of the arc, the strategies based on the COB algorithm give significantly worse results than the ones based on other IP techniques. It can also be noted that the error using the *Reference* strategy increases significantly over time. This is caused by the accuracy of the ephemerides stored on-board, which degrades as time goes by because of uncertainties. From a pointing perspective, if *Reference* is used as a nominal strategy for the pointing, D1 could be lost by the navcam FOV towards the end of the arc. The last portion of the arc coincides with the CubeSat getting closer to the system, which causes a general increase in the pointing error for all strategies considered.

Only for COB-based strategies the performance instead improves. This is explained by the fact that only towards the end when the apparent dimension of D1 increases and the body is seen at low phase angles, the COB performance aligns with that of the other IP methods. This causes the performance of the COB-based *Predicted* and *Tracking* strategies to align with the other ones.

A different trend is observed for the on-board position reconstruction error in Fig. 12. In this case, three different phases are identified for the strategies using the EKF. At first, the error rapidly decreases at the beginning of the arc, after initialization, showing quick convergence of the EKF. This phase is then followed by one in which the errors display a steady but constant increase. Finally, towards the end of the arc, a rapid drop can be observed. On the other hand, the error with the *Reference* strategy, which uses the ephemerides stored on-board, shows a steady but constant increase throughout the entire arc.

As already observed, the accuracy of the IP method used consistently affects the performance of the EKF, which in all cases considered performed better than the reference scenario. Lastly, it is noted that the different trends between the EKF error in Fig. 11 and the *Predicted* one in Fig. 12 is explained by the fact that the majority of the former is expressed in the navcam boresight direction. Since this does not actively contribute to the pointing error, different trends are observed over ε_θ and ε_p.
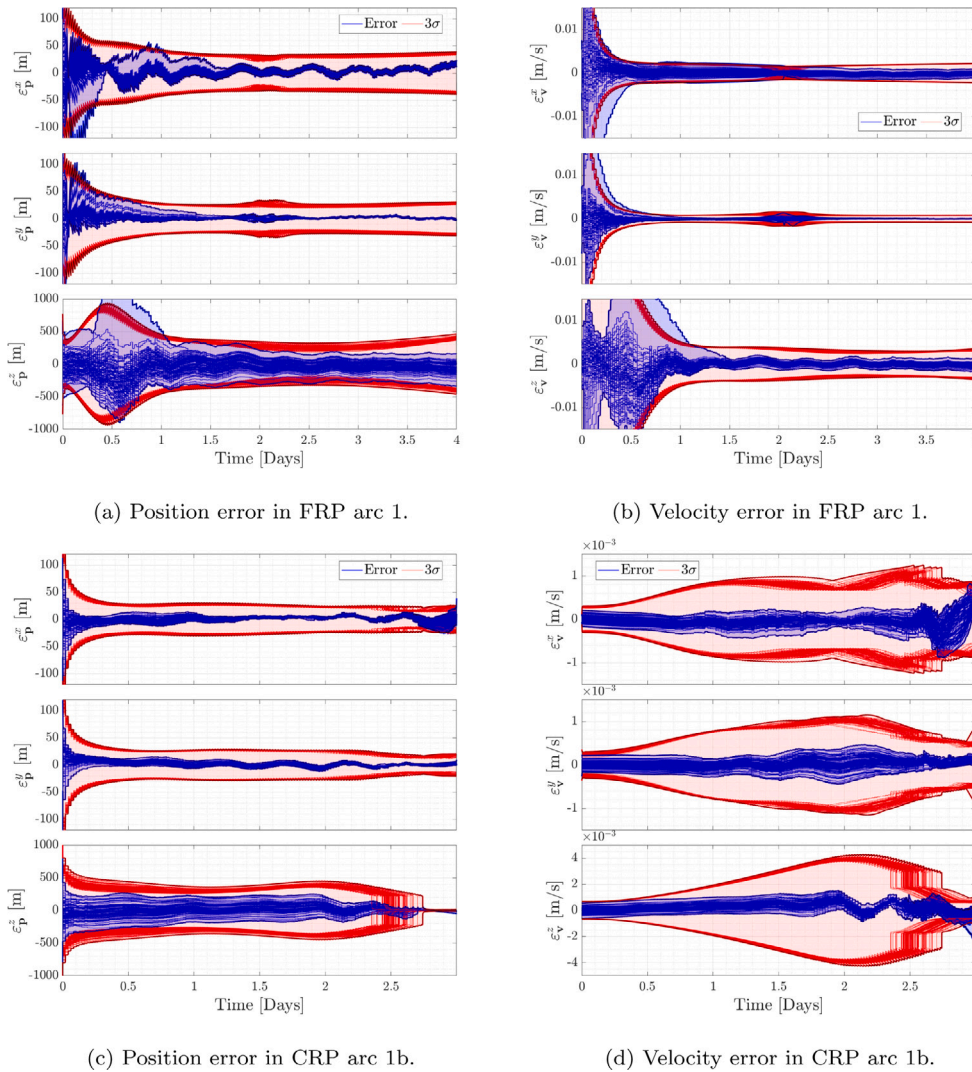
(a) Position error in FRP arc 1.

(b) Velocity error in FRP arc 1.

(c) Position error in CRP arc 1b.

(d) Velocity error in CRP arc 1b.

Fig. 13. Performance of the EKF in the MC campaign.

5.4. Monte Carlo

The MC simulations are devised to test the overall robustness of the system to uncertainty in the initial conditions and the different scenarios these may take the CubeSat into.

In Fig. 13, it is possible to see the error in the camera frame of the position and velocity estimates of the on-board EKF on the 100 test cases. Apart from a few isolated cases, the filter produces robust and consistent results. In FRP arc 1, only one case exits the 3σ bounds before being quickly recovered. In CRP arc 1b, the errors tend to increase as the CubeSat gets closer to D1. In this case, the beneficial effect of the LiDAR is clearly visible towards the end of the arc, especially in the z component, which represents the navcam boresight direction.

Fig. 14 shows the min–max envelopes (represented by the black area between the maxima and minima of the 100 cases) of the on-board position estimation error, the pointing accuracy, and the IP performance over time together with their corresponding mean values (blue line) and mission requirements, $R1$, $R2$, and $R3$ (represented by green dashed lines). In the majority of the samples considered in the test campaigns, the metrics are well below the required threshold illustrated in Table 1, with just a few exceptions which are temporally isolated. It is interesting to note a periodic pattern of approximately 12 hours in the pointing errors in both campaigns. This is explained by the relative motion of D1 moving in a circular orbit with a radius of roughly 10 m around the barycenter of the binary system, whose

period is consistent with the one visible in Figs. 14(a) and 14(b). Since this motion is neglected when the pointing direction is computed, it is picked up as a pointing error. Finally, in Figs. 14(c) and 14(d) some discontinuities are observed which are explained by changes of γ_{nav}.

5.5. Logics

Finally, an example of the application of FDIR logics is reported in Fig. 15 for a scenario in which the navcam is temporarily forced off after about 2.5 hours and then turned back on after 10 hours. Through the different modes γ_{gnc} and submodes γ_{nav}, γ_{ekf} and γ_{gui} it is possible to test the reaction of the GNC system to this simulated event. Initially, the system behaves nominally with the guidance submode switching to *Tracking* at initialization and then to *Predicted*. Similarly, the navigation submode switches to *Navigation from ephemerides* and then to *Navigation from EKF*. In this case, LiDAR measurements are not available because of the distance from the system. As soon as the navcam is turned off, the EKF stops using measurements and remains in *Propagation only*. The guidance and navigation submodes initially remain in *Predicted* and *Navigation from EKF*, respectively. This is an intended behavior to avoid unnecessary slew maneuvers in case the navcam quickly resumes working. After a while, the guidance submode automatically goes down to *Reference* and the navigation submode to *Navigation from ephemerides*. These submodes do not require the navcam to work, as they rely only on data stored on-board. As soon as the navcam is turned back on, the system reacts by returning to nominal operative conditions.
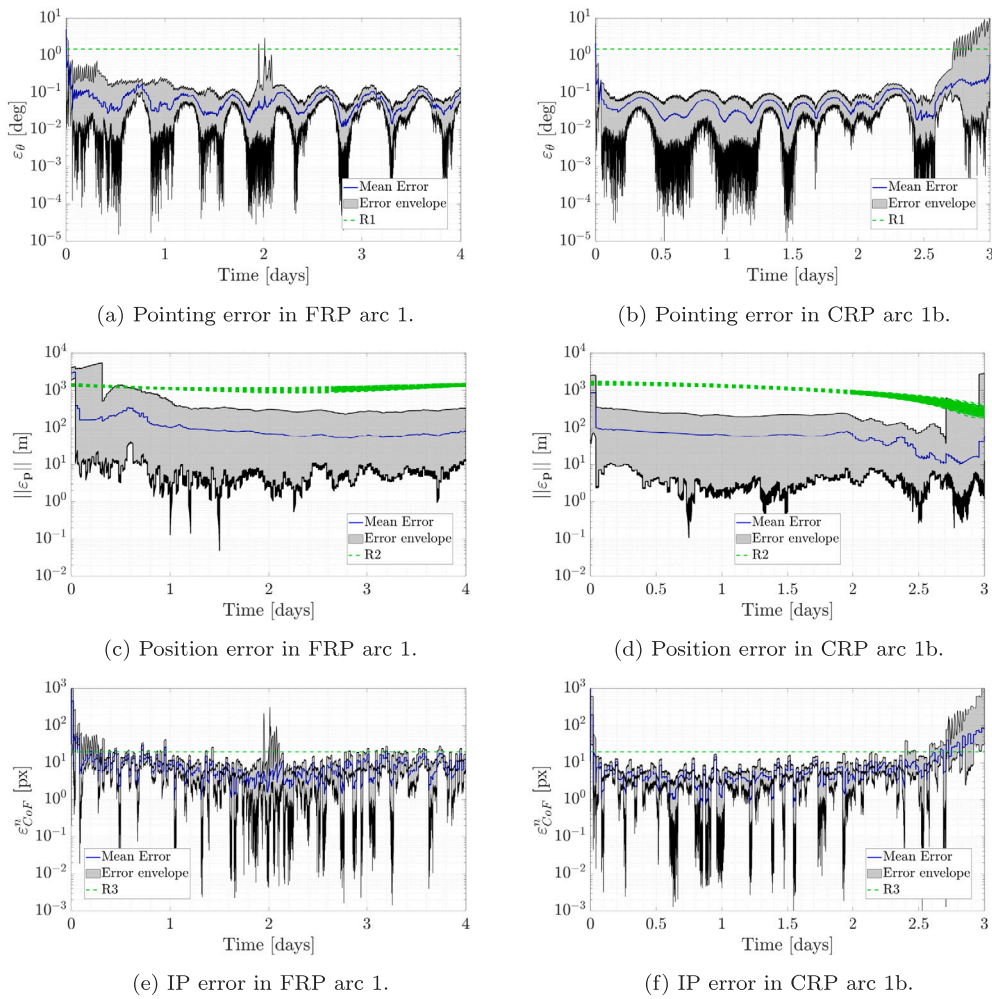
(a) Pointing error in FRP arc 1.

(b) Pointing error in CRP arc 1b.

(c) Position error in FRP arc 1.

(d) Position error in CRP arc 1b.

(e) IP error in FRP arc 1.

(f) IP error in CRP arc 1b.

Fig. 14. Pointing error, on-board position reconstruction error, and IP error of the MC campaign. (For interpretation of the references to color in this figure legend, the reader is referred to the web version of this article.)

6. Conclusions

This work has provided a detailed overview of the Milani mission architecture with a focus on image processing and guidance, navigation, and control system design and performance analysis.

Both the IP and GNC algorithms have been automatically translated to C code using the MathWorks Embedded Coder[4] and are currently being integrated with the Milani flight software. The autocoding process has been demonstrated to be a critical element to enable rapid design and deployment of the algorithms presented in this work. Few lessons learned have been gained from this experience. For example, not all Matlab/Simulink functions are supported for autocode generation, therefore some of them may need to be manually coded to comply with the coder requirements. Identifying such functions in the early stages of the project during algorithm development is essential. Additionally, whenever possible, it has been observed to be preferable to use Simulink blocks rather than Matlab code, as they are optimized for efficient C code generation and faster execution time. Finally, the usage of Simulink blocks also optimizes memory utilization. This may be critical, especially for IP algorithms, that often require significant amounts of random access memory (RAM) to process images.

Finally, in this work it has been shown that the design and performance of the IP and GNC systems is compliant with the applicable requirements, especially in challenging arcs. The performance of the designed vision-based GNC system assures adequate pointing and control of the platform in the Didymos environment, ensuring the mission feasibility in flying a miniaturized platform in such a harsh environment.

Declaration of competing interest

The authors declare that they have no known competing financial interests or personal relationships that could have appeared to influence the work reported in this paper.

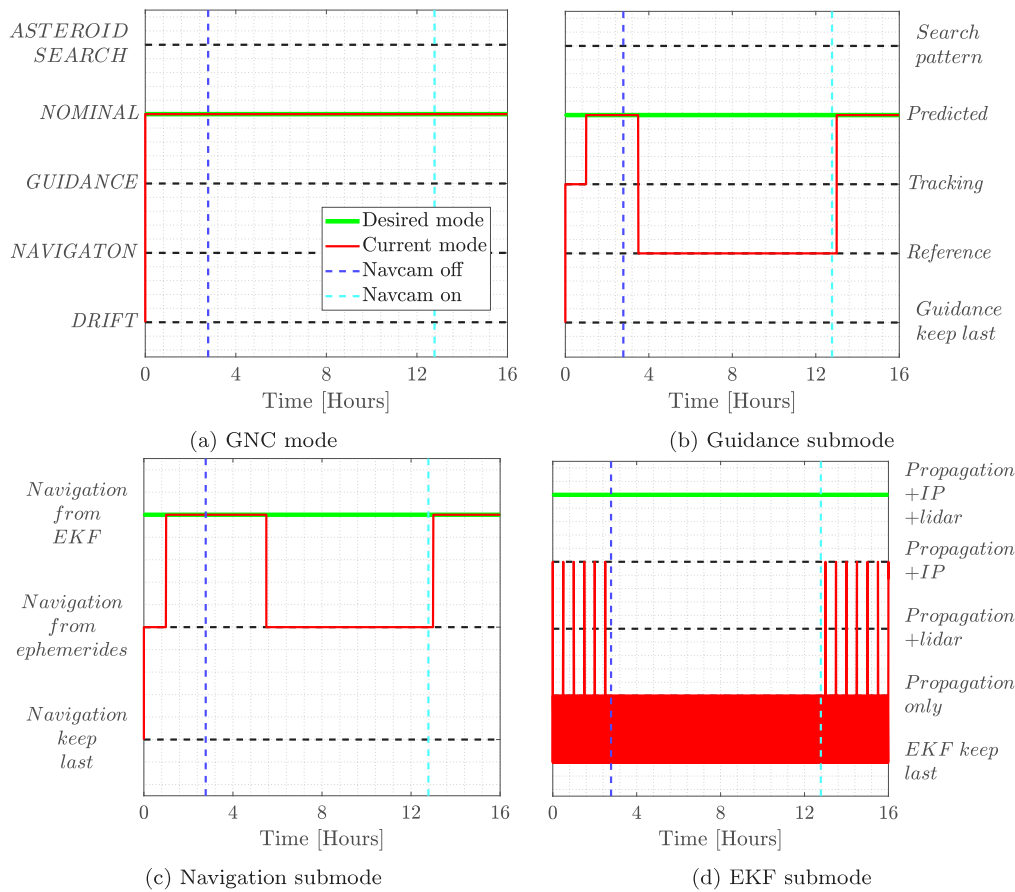[4] https://www.mathworks.com/products/embedded-coder.html

Fig. 15. Response of the different operative modes of the GNC after a simulated navigation navcam anomaly. The navcam is turned off after about 2.5 h, then it is turned back on after 10 h.

References

[1] K.-H. Glassmeier, H. Boehnhardt, D. Koschny, E. Kührt, I. Richter, The Rosetta mission: flying towards the origin of the solar system, Space Sci. Rev. 128 (1) (2007) 1–21, http://dx.doi.org/10.1007/s11214-006-9140-8.

[2] M. Yoshikawa, J. Kawaguchi, A. Fujiwara, A. Tsuchiyama, Hayabusa sample return mission, Asteroids IV 1 (2015) 397–418, http://dx.doi.org/10.2458/azu_uapress_9780816532131-ch021.

[3] S.-i. Watanabe, Y. Tsuda, M. Yoshikawa, S. Tanaka, T. Saiki, S. Nakazawa, Hayabusa2 mission overview, Space Sci. Rev. 208 (1) (2017) 3–16, http://dx.doi.org/10.1007/s11214-017-0377-1.

[4] D. Lauretta, S. Balram-Knutson, E. Beshore, W. Boynton, C.D. d'Aubigny, D. DellaGiustina, H. Enos, D. Golish, C. Hergenrother, E. Howell, et al., OSIRIS-REx: sample return from asteroid (101955) Bennu, Space Sci. Rev. 212 (1) (2017) 925–984, http://dx.doi.org/10.1007/s11214-017-0405-1.

[5] C. Snodgrass, G.H. Jones, The European Space Agency's Comet Interceptor lies in wait, Nature Commun. 10 (1) (2019) http://dx.doi.org/10.1038/s41467-019-13470-1.

[6] P. Michel, M. Küppers, I. Carnelli, The Hera mission: European component of the ESA-NASA AIDA mission to a binary asteroid, in: COSPAR Scientific Assembly, Pasadena, California, 2018, pp. 1–42.

[7] H.F. Levison, C.B. Olkin, K.S. Noll, S. Marchi, J.F.B. III, E. Bierhaus, R. Binzel, W. Bottke, D. Britt, M. Brown, M. Buie, P. Christensen, J. Emery, W. Grundy, V.E. Hamilton, C. Howett, S. Mottola, M. Pätzold, D. Reuter, J. Spencer, T.S. Statler, S.A. Stern, J. Sunshine, H. Weaver, I. Wong, Lucy Mission to the Trojan Asteroids: Science Goals, Planet. Sci. J. 2 (5) (2021) 171, http://dx.doi.org/10.3847/psj/abf840.

[8] D.J. Scheeres, J.W. McMahon, E.B. Bierhaus, J. Wood, L.A.M. Benner, C.M. Hartzell, P. Hayne, R. Jedicke, L. Le Corre, A. Meyer, S. Naidu, P. Pravec, M. Ravine, K. Sorli, Janus: A NASA SIMPLEx mission to explore two NEO Binary Asteroids, in: 7th IAA Planetary Defense Conference, 2021, p. 55.

[9] T.R. Lockett, J. Castillo-Rogez, L. Johnson, J. Matus, J. Lightholder, A. Marinan, A. Few, Near-Earth Asteroid Scout Flight Mission, IEEE Aerosp. Electron. Syst. Mag. 35 (3) (2020) 20–29, http://dx.doi.org/10.1109/MAES.2019.2958729, https://ieeexplore.ieee.org/document/9076194.

[10] F. Topputo, Y. Wang, C. Giordano, V. Franzese, H. Goldberg, F. Perez-Lissi, R. Walker, Envelop of reachable asteroids by M-ARGO CubeSat, Adv. Space Res. 67 (12) (2021) 4193–4221, http://dx.doi.org/10.1016/j.asr.2021.02.031.

[11] R. Walker, D. Binns, C. Bramanti, et al., Deep-space CubeSats: thinking inside the box, Astron. Geophys. 59 (5) (2018) 5–24, http://dx.doi.org/10.1093/astrogeo/aty237.

[12] A. Cervone, F. Topputo, S. Speretta, A. Menicucci, E. Turan, P. Di Lizia, M. Massari, V. Franzese, C. Giordano, G. Merisio, et al., LUMIO: A CubeSat for observing and characterizing micro-meteoroid impacts on the Lunar far side, Acta Astronaut. 195 (2022) 309–317, http://dx.doi.org/10.1016/j.actaastro.2022.03.032.

[13] P. Michel, A. Cheng, M. Küppers, Asteroid Impact and Deflection Assessment (AIDA) mission: science investigation of a binary system and mitigation test, in: European Planetary Science Congress, vol. 10, 2015, pp. 123–124.

[14] A.S. Rivkin, N.L. Chabot, A.M. Stickle, C.A. Thomas, D.C. Richardson, O. Barnouin, E.G. Fahnestock, C.M. Ernst, A.F. Cheng, S. Chesley, S. Naidu, T.S. Statler, B. Barbee, H. Agrusa, N. Moskovitz, R.T. Daly, P. Pravec, P. Scheirich, E. Dotto, V.D. Corte, P. Michel, M. Küppers, J. Atchison, M. Hirabayashi, The double asteroid redirection test (DART): Planetary defense investigations and requirements, Planet. Sci. J. 2 (5) (2021) 173, http://dx.doi.org/10.3847/PSJ/ac063e, https://iopscience.iop.org/article/10.3847/PSJ/ac063e/meta.

[15] A.F. Cheng, A.S. Rivkin, P. Michel, J. Atchison, O. Barnouin, L. Benner, N.L. Chabot, C. Ernst, E.G. Fahnestock, M. Kueppers, P. Pravec, E. Rainey, D.C. Richardson, A.M. Stickle, C. Thomas, AIDA DART asteroid deflection test: Planetary defense and science objectives, Planet. Space Sci. (ISSN: 0032-0633) 157 (2018) 104–115, http://dx.doi.org/10.1016/j.pss.2018.02.015.

[16] E. Dotto, V. Della Corte, M. Amoroso, I. Bertini, J. Brucato, A. Capannolo, B. Cotugno, G. Cremonese, V. Di Tana, I. Gai, et al., LICIACube-the light Italian cubesat for imaging of asteroids in support of the NASA dart mission towards asteroid (65803) didymos, Planet. Space Sci. (2021) 105185, http://dx.doi.org/10.1016/j.pss.2021.105185.

[17] P. Michel, M. Küppers, A.C. Bagatin, B. Carry, S. Charnoz, J. de Leon, A. Fitzsimmons, P. Gordo, S.F. Green, A. Hérique, M. Juzi, Ö. Karatekin, T. Kohout, M. Lazzarin, N. Murdoch, T. Okada, E. Palomba, P. Pravec, C. Snodgrass, P. Tortora, K. Tsiganis, S. Ulamec, J.-B. Vincent, K. Wünnemann, Y. Zhang, S.D. Raducan, E. Dotto, N. Chabot, A.F. Cheng, A. Rivkin, O. Barnouin, C. Ernst, A. Stickle, D.C. Richardson, C. Thomas, M. Arakawa, H. Miyamoto, A. Nakamura,

S. Sugita, M. Yoshikawa, P. Abell, E. Asphaug, R.-L. Ballouz, W.F. Bottke, D.S. Lauretta, K.J. Walsh, P. Martino, I. Carnelli, The ESA Hera mission: Detailed characterization of the DART impact outcome and of the binary asteroid (65803) didymos, Planet. Sci. J. 3 (7) (2022) 160, http://dx.doi.org/10.3847/psj/ac6f52.

[18] H. Goldberg, O. Karatekin, B. Ritter, et al., The Juventas CubeSat in Support of ESA's Hera Mission to the Asteroid Didymos, in: Small Satellite Conference, in: Logan, Utah, 2019, pp. 1–7.

[19] F. Ferrari, V. Franzese, M. Pugliatti, C. Giordano, F. Topputo, Preliminary mission profile of Hera's Milani CubeSat, Adv. Space Res. (ISSN: 0273-1177) 67 (6) (2021) 2010–2029, http://dx.doi.org/10.1016/j.asr.2020.12.034.

[20] T. Kohout, M. Cardi, A. Näsilä, E. Palomba, F. Topputo, The Milani team, Milani CubeSat for ESA Hera mission, in: European Planetary Science Congress 2021, in: EPSC2021-732, 2021, pp. 1–3, http://dx.doi.org/10.5194/epsc2021-732.

[21] F. Dirri, E. Palomba, A. Longobardo, D. Biondi, A. Boccaccini, A. Galiano, E. Zampetti, B. Saggin, D. Scaccabarozzi, J. Martin-Torres, VISTA Instrument: A PCM-Based Sensor for Organics and Volatiles Characterization by Using Thermogravimetric Technique, in: 2018 5th IEEE International Workshop on Metrology for AeroSpace (MetroAeroSpace), IEEE, 2018, pp. 150–154, http://dx.doi.org/10.1109/MetroAeroSpace.2018.8453532, https://ieeexplore.ieee.org/document/8453532.

[22] F. Ferrari, V. Franzese, M. Pugliatti, C. Giordano, F. Topputo, Trajectory Options for Hera's Milani CubeSat Around (65803) Didymos, J. Astronaut. Sci. (2021) http://dx.doi.org/10.1007/s40295-021-00282-z.

[23] M. Pugliatti, V. Franzese, F. Topputo, Data-Driven Image Processing for On-board Optical Navigation Around a Binary Asteroid, J. Spacecr. Rockets (2022) 943–959, http://dx.doi.org/10.2514/1.a35213.

[24] M. Pugliatti, V. Franzese, A. Rizza, F. Piccolo, C. Bottiglieri, C. Giordano, F. Ferrari, F. Topputo, Design of the on-board image processing of the Milani mission, in: 2022 AAS GN&C Conference, in: Breckenridge, Colorado, 2022, pp. 1–20.

[25] F. Piccolo, M. Pugliatti, P. Panicucci, F. Topputo, Toward verification and validation of the Milani Image Processing pipeline in the hardware-in-the-loop testbench TinyV3RSE, in: AAS/GNC 2022, 2022, pp. 1–22.

[26] M. Pugliatti, A. Rizza, F. Piccolo, V. Franzese, C. Bottiglieri, C. Giordano, F. Ferrari, F. Topputo, The Milani mission: overview and architecture of the optical-based GNC system, in: Scitech 2022, 2022, pp. 1–20, http://dx.doi.org/10.2514/6.2022-2381.

[27] J.R. Carpenter, C.N. D'Souza, Navigation filter best practices, Tech. rep., 2018, TP-2018-219822: https://ntrs.nasa.gov/archive/nasa/casi.ntrs.nasa.gov/20180003657.pdf20180003657.

[28] A. Rizza, F. Piccolo, M. Pugliatti, P. Panicucci, F. Topputo, Hardware-in-the-loop simulation framework for CubeSats proximity operations: application to the Milani mission, in: 73rd International Astronautical Congress (IAC 2022), Paper IAC-22,C1,3,X69254, Paris, France, 2022.

[29] C. Bottiglieri, F. Piccolo, M. Pugliatti, V. Franzese, C. Giordano, F. Ferrari, F. Topputo, Mission Analysis and Navigation Assessment for Hera's Milani CubeSat, in: 2022 4S Symposium, in: Vilamoura, Portugal, 2022, pp. 1–12.